GEOCHEMISTRY

Sulfur disproportionation in deep COHS slab fluids drives mantle wedge oxidation

Andrea Maffeis[1]*, Maria Luce Frezzotti[2]*, James Alexander Denis Connolly[3], Daniele Castelli[1], Simona Ferrando[1]

Sulfur degassed at volcanic arcs calls for dissolved sulfate ions (S^{6+}) released by subduction-zone fluids, oxidizing (in association with carbon) the subarc mantle, but sulfur speciation in subduction fluids at subarc depths remains unclear. We apply electrolytic fluid thermodynamics to model the dissolution behavior of pyrite in metacarbonate sediments as a function of *P*, *T* and rock redox state up to 4.3 gigapascals and 730°C. At subarc depth and the redox conditions of the fayalite-magnetite-quartz oxygen buffer, pyrite dissolution releases oxidized sulfur in fluids by disproportionation into sulfate, bisulfite, and sulfide species. These findings indicate that oxidized, sulfur-rich carbon-oxygen-hydrogen-sulfur (COHS) fluids form within subducting slabs at depths greater than 100 kilometers independent from slab redox state and that sulfur can be more effective than the concomitantly dissolved carbon at oxidizing the mantle wedge, especially when carbonates are stable.

INTRODUCTION

Magmas at convergent margins are more oxidized than those generated at mid-ocean ridges and release CO_2 and SO_2 to the atmosphere by volcanic emissions (*1*–*3*), which are crucial climate-forcing gasses (*4*, *5*). Their origin is intimately linked to subduction tectonics, responsible for cycling volatile elements into Earth's mantle. Whether arc magma oxidized nature is acquired at the mantle source, by subduction fluids, or later, on the ascent through the mantle and the crust is currently debated (*6*–*11*). The subarc mantle is generally more oxidized than the oceanic or ancient cratonic mantle (fig. S1) (*12, 13*). Redox-sensitive elements, such as C and S, transported by fluids released during deep subduction, can potentially generate the high redox conditions—expressed in terms of oxygen fugacity (fo_2)—proposed for the subarc mantle wedge (*12, 13*).

In subducting lithosphere, sulfur mineral stability depends on initial sulfur content, rock composition (e.g., serpentinites, eclogites, and metasediments), pressure-temperature (*P*-*T*) path, and redox conditions. In serpentinites and eclogites, thermodynamic modeling predicts pyrrhotite at forearc conditions (*14*–*17*). In eclogites and serpentinites, pyrite is thermodynamically predicted to be the most common sulfur phase at prevailing fo_2 conditions during subarc metamorphism along cold subduction geotherms [$<\Delta FMQ + 1$; fo_2 expressed as the logarithmic unit difference relative to the FMQ (fayalite-magnetite-quartz buffer)] (*14*–*17*). Anhydrite is predicted to be stable at markedly high fo_2 conditions or above temperatures of the forearc to subarc transition (i.e., $>\Delta FMQ + 2$) (*14*–*16*).

Field evidence in exhumed (ultra)high-pressure (H*P*/UH*P*) metamorphic rocks (i.e., eclogites, metasediments, and serpentinites exhumated from depths greater than 70 to 80 km) indicates that although pyrrhotite might be present in some serpentinites, pyrite (±chalcopyrite) is commonly present in association with carbonates (±graphite) in most rock types at subarc depths [e.g., (*18*–*24*)]. Sulfates, although present in sediments and altered oceanic crust (AOC) at the trench (*25*), are absent in the metamorphic record from the early subduction stages (*20*, *22*, *24*). This evidence led several researchers to propose that oxidized sulfur fluxes from the slab to the overlying mantle wedge, the source of arc magmas, could be negligible (*23*, *24*, *26*). However, high S^{6+}/S_{tot} in H*P*/UH*P* slab fluids cast doubt on the view that reduced aqueous sulfur is released from pyrite dissolution. For example, sulfate and bisulfate are dominant sulfur species in aqueous fluid inclusions in exhumed metamorphic rocks, along with carbonate ions, CO_2, and carboxylic compounds, often associated with microdiamonds (*27, 28*).

Although recent work has shed light on the oxidized carbon speciation in deep slab aqueous fluids at variable *P*-*T*, rock composition, and, consequently, redox conditions [e.g., (*26*–*32*)], relatively few data are available on aqueous sulfur speciation, along deep subduction *P*-*T* paths (*14*, *24*, *33*). Even less is known about the interplay of S and C in aqueous fluids in the deep subduction environment (*15*, *16*), preventing us from fully understanding redox processes in the subarc mantle.

In this study, we explore, using electrolytic fluid thermodynamic modeling, the dissolution mechanisms and the redox-dependent speciation of S and C in aqueous fluids during subduction at subarc depths within carbonate metasediments in the fo_2 range from $\Delta FMQ - 1$ to $\Delta FMQ + 1$. We performed deep fluid thermodynamic modeling in metasediments since these rocks, despite their small volume compared to the rest of the slab, potentially behave as powerful "oxidative fluid filters" (*34*) at the top of a downgoing slab, imprinting their geochemical fingerprint to fluids leaving the slab (see Supplementary Text for further information) (*34*–*36*). We find that, as observed in further modeling in other slab lithologies, at high *P* and *T* (3 to 4.3 GPa and ~560° to 730°C), pyrite dissolution in aqueous fluids occurs by S^{1-} disproportionation into sulfate, bisulfite, and sulfide species. Sulfur disproportionation in internally and externally derived slab COHS fluids expands the *P*-*T*-fo_2 conditions for slab release of highly oxidizing fluids to the overlying mantle wedge.

RESULTS

S and C speciation in metacarbonate fluids

Tracing the speciation of metasedimentary sulfur and carbon in COHS fluid at depths first requires knowledge of the *P*-*T*-fo_2 conditions at which fluids equilibrated before entering the mantle wedge. Thus, we chose a UHP impure calcitic-dolomitic marble (sample

---

[1]Università di Torino, Dipartimento di Scienze della Terra, Torino, Italy. [2]Università degli Studi di Milano-Bicocca, Dipartimento di Scienze dell'Ambiente e della Terra, Milano, Italy. [3]ETH-Zürich, Department of Earth Sciences, Institute for Geochemistry and Petrology, Zürich, Switzerland.
*Corresponding author. Email: andrea.maffeis@unito.it (A.M.); maria.frezzotti@unimib.it (M.L.F.)

DM675) from the Dora-Maira Massif (DM; Western Alps) as a possible composition of a carbonate-rich metasediment (composing up to 72 vol % of the subducting sediments column) (*37*) along deep cold subduction path (*38*) (DM in Fig. 1A; compare fig. S2 and tables S1 and S2; and see Supplementary Text). The rock consists of calcite (ex-aragonite), dolomite, forsterite, and diopside and has experienced multiple syn-subduction carbonate dissolution-precipitation events (*38*–*40*).

We modeled equilibrium metacarbonate phase relations and fluid chemistry in the subarc segment of the DM *P*-*T* path from 3 GPa (or about 100 km in depth) and 560°C to 4.3 GPa (or about 140 km in depth) and 730°C in a fo_2 range relevant for monitoring pyrite and anhydrite dissolution at the redox conditions hypothesized to prevail in metasediments (i.e., ΔFMQ − 1, FMQ, and ΔFMQ + 1; Fig. 1B; compare fig. S3A for the complete phase diagram). Aragonite and dolomite are stable at the investigated P-T-fo_2 conditions. In contrast, anhydrite substitutes pyrite at ΔFMQ + 0.5 at 560°C and 3 GPa and right above the FMQ at 730°C and 4.3 GPa (Fig. 1B). In metacarbonates, high Ca contents expand anhydrite stability field to more reduced conditions, unlike mafic and ultramafic rocks (*16*, *41*).

Carbonate and anhydrite/pyrite dissolution modeling (Fig. 1B) reveals a decoupled—P-T-fo_2–dependent—C and S solubility and speciation in the aqueous fluid. Along the considered *P*-*T* path, at ΔFMQ + 1, anhydrite dissolution increases with increasing *P* and *T* up to 650°C and 3.8 GPa, decreasing at higher *P* and *T* (Fig. 2A). Aqueous sulfur speciation is dominated by sulfate species (up to 1.32 mol % at 730°C and 4.3 GPa; $CaSO_{4,aq}$, SO_4^{2-}, and HSO_4^-) with subordinate sulfite (up to 0.12 mol %; HSO_3^-) and traces of sulfide ions (Fig. 2, C and D). The corresponding fluid S average valence state (AVS) is about +5.75 (fig. S4A). At lower fo_2, sulfur in aqueous fluids is controlled by pyrite dissolution. We observe that at FMQ, thermodynamic modeling predicts dominant amounts of dissolved sulfate (up to 1.20 mol %; Fig. 2, C to F), with subordinate intermediate sulfite (up to 0.35 mol %) and sulfide species (H_2S and HS^- up to 0.31 mol %), and traces of radical S_3^-. As *P* and *T* increase from 560°C and 3 GPa to 730°C and 4.3 GPa, the corresponding oxidized sulfur AVS rises considerably from +0.38 to +4.27 (fig. S4A). At even lower fo_2 conditions (ΔFMQ − 1), although sulfide species dominate in the fluid (up to 0.80 mol %) and leading to a reduced S AVS that varies from −1.95 to −1.47 (fig. S4A), dissolved sulfate and sulfite species and sulfur radicals are predicted to be up to 0.03 mol % (Fig. 2, C to F) along the considered *P*-*T* path.

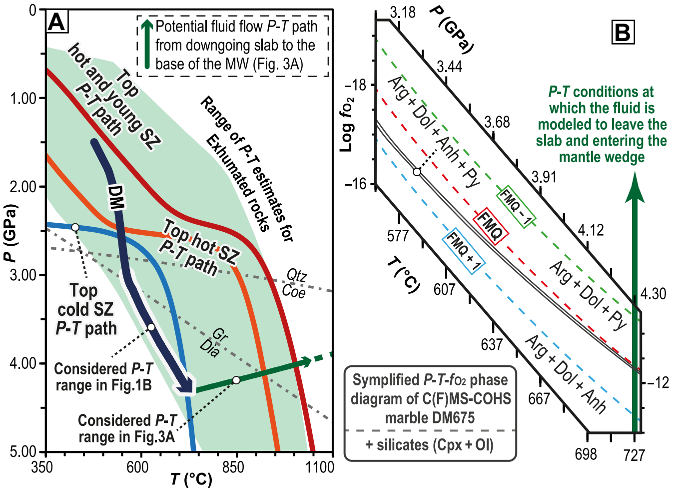

Fig. 1. Modeled *P-T* conditions and simplified phase diagram. (**A**) Used *P-T* path (dark blue) of the Dora-Maira metamorphic complex (*77*) shown together with the reference *P-T* conditions of top of cold (light blue), hot modern subduction zones (SZ) (red and dark red) (*78*), and exhumed rocks from inactive subduction zones (light green field) (*79*). Dark green line represents the *P-T* path of the fluid ascent from the slab into the deeper portion of the mantle wedge (MW) (*66*), used to calculate mantle $T(P)$-fo_2 phase equilibria in Fig. 3A. (**B**) Simplified P-T-fo_2 phase diagram (fig. S3 for complete diagram) shows the relevant topological features for C and S redox-sensitive mineral phases. Mineral abbreviations after (*80*).

At all considered fo_2 conditions, carbon solubility (Fig. 2B) and oxidized species (C^{4+}) in fluids increase, at increasing *P* and *T*. At 730°C and 4.3 GPa, bicarbonate ions dominate (up to 1.34 mol %), with traces of CO_2 (up to 0.08 mol %) and carbonate ions (up to 0.04 mol %; Fig. 2, G and H). Carboxylic compounds (i.e., characterized by having a carboxyl group), with carbon in multiple intermediate valence states (e.g., C^{3+}, C^{2+}, and C^{3-}), increase at decreasing fo_2: From ΔFMQ + 1 to ΔFMQ − 1 conditions, carboxylic compounds increase by one order of magnitude (from 0.001 to 0.012 mol %). Traces of hydrocarbons are stable only at ΔFMQ − 1 (Fig. 2, I and J). Corresponding carbon AVS slightly decreases from +3.98 to +3.83 with decreasing fo_2 (fig. S4B).

In our modeling, the fluid speciation of dissolved S and C is decoupled. For example, while carbon is mostly oxidized (from dissolving carbonates), sulfur at neutral redox conditions (i.e., FMQ) is predicted as multiple ionic species. The carbon and sulfur speciation in fluids during pyrite and carbonate (aragonite) dissolution at ~730°C and ~4.3 GPa and at the FMQ can be schematized with a type reaction

$$CaCO_3 + 3FeS_2 + 3H_2O + 2O_2 = HCO^-_{3,aq} + CaSO_{4,aq} + HSO^-_3 + 4HS^-_{aq} + 3Fe^{2+}_{Sil}$$

Carbon dissolves into dominant bicarbonate ions, and sulfur speciates as sulfate, sulfite, and sulfide. Although considered in the calculations, intermediate radicals, such as S_3^- (*42*), are present in very subordinate amounts at the considered P-T-fo_2 conditions. Thus, aqueous species covering the entire range of S valence states (from +6 to −2, even with intermediate values) indicate that sulfur released at high *P* and *T* by pyrite dissolution undergoes disproportionation reactions.

The oxidizing capacity of COHS fluids buffered by metacarbonate sediments

The predicted oxidized speciation by sulfur disproportionation on pyrite dissolution in metacarbonates has implications for the fluid potential to initiate redox reactions within the overlying mantle wedge. To investigate the redox capacity transferable between different chemical systems, specific variables, such as the specific redox budget (RB hereafter; see Materials and Methods) (*43*, *44*), are better suited than fo_2 to evaluate the transferable oxidative capacity between two separate systems (e.g., from the slab toward the overlying mantle) (*43*, *45*).

In the modeled fluids, the redox capacity is controlled by C and S since the contribution of O, H, and Fe is negligible (figs. S5 and S6, G to N). The calculated fluid RB simulates the potential redox impact of the fluid upon interaction with a depleted mid ocean ridge basalt (MORB) mantle (DMM) (*46*). The P-T-fo_2 mantle model reported in Fig. 3A (at *P*-*T* conditions selected to be representative for a suprasubduction mantle, from 750°C and 4.3 GPa to 1010°C and

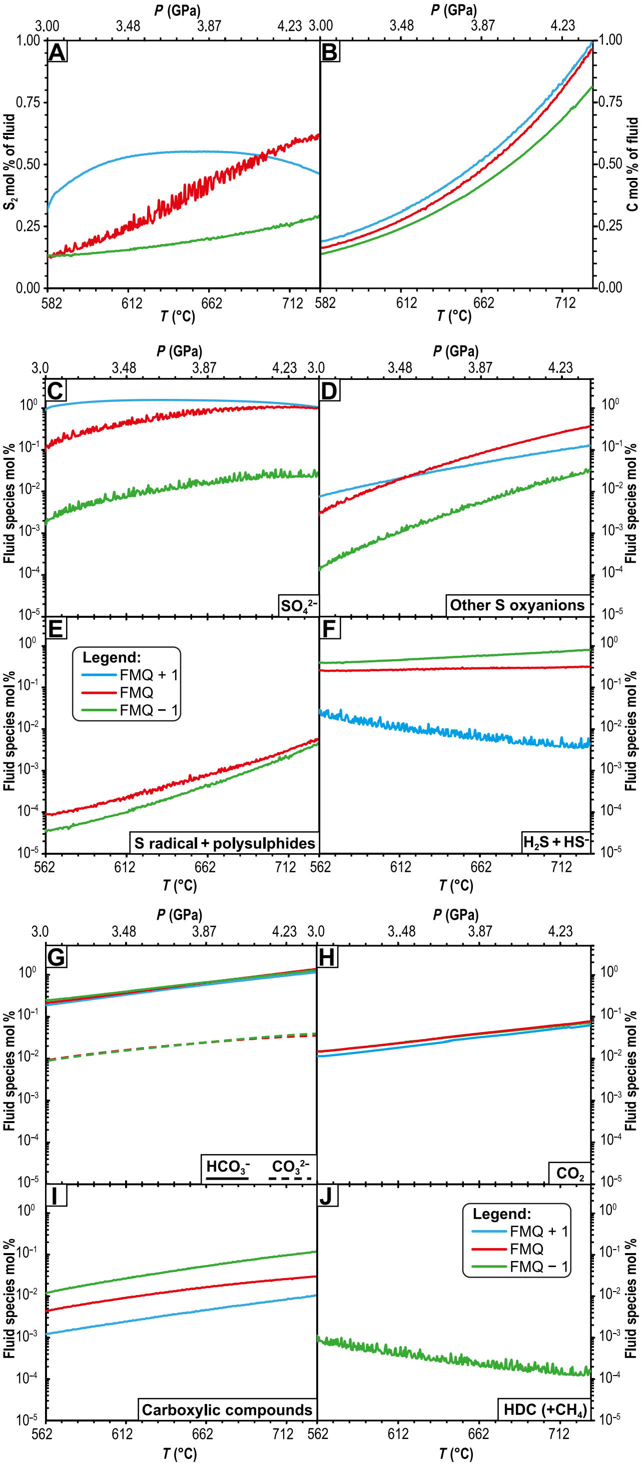

Fig. 2. Chemistry of aqueous solute-bearing COHS fluids as a function of *P-T-$f\mathrm{O}_2$*. (**A** and **B**) S and C solubility in solute-bearing COHS fluids as a function of *P-T-$f\mathrm{O}_2$*. (**C** to **J**) Evolution of C and S species groups as a function of *P-T-$f\mathrm{O}_2$*. The species have been grouped according to chemical similarities to improve the legibility of C and S speciation data (see table S3 for the groups' definitions).

4 GPa) shows that the DMM should be located on the reduced side the enstatite-magnesite-olivine-diamond oxygen buffer (EMOD) (*47*): in the diamond (C^0) and pyrrhotite (S^{2-}) stability field (red band in Fig. 2A). Similarly, at the same *P-T* conditions, the oxidized side of the EMOD buffer, the carbonate (C^{4+}) and pyrrhotite stability field, should be representative for the $f\mathrm{O}_2$ conditions of the mantle wedge (yellow band in Fig. 3A).

In the subducting slab, anhydrite dissolution (at ΔFMQ + 1) climaxes at 650°C and 3.8 GPa and decreases at higher *P* and *T*. Relative to a diamond-pyrrhotite–bearing mantle, this results in an S oxidizing capacity decreasing from a maximum of +6.7 down to +5.4 e^- mol/kg$_{\text{fluid}}$, from 3.8 to 4.3 GPa (i.e., from 90% down to 70% of total fluid RB; Fig. 3B and fig. S6A). A notable observation from the dataset is that fluids generated during pyrite dissolution at lower $f\mathrm{O}_2$ (i.e., FMQ) have comparable S oxidizing capacity to that at ΔFMQ + 1. Sulfur disproportionation highly increases the fluid oxidation capacity from +0.48 e^- mol/kg$_{\text{fluid}}$ at 560°C and 3 GPa to +5.7 e^- mol/kg$_{\text{fluid}}$ at 730°C and 4.3 GPa (i.e. from 50% up to 70% of total fluid RB; Fig. 3B and fig. S6B). At ΔFMQ − 1, pyrite dissolution still results in an oxidizing fluid capacity, but one order of magnitude is lower than at the FMQ (i.e., up to +0.2 e^- mol/kg$_{\text{fluid}}$ or <8% of total fluid RB at 730°C and 4.3 GPa; Fig. 3B and fig. S6B). In modeled COHS fluids, at 730°C and 4.3 GPa, carbon oxidizing RB, calculated relative to a diamond-pyrrhotite–bearing subarc mantle, increases from +2.4 to +3.3 e^- mol/kg$_{\text{fluid}}$ as the sediment's $f\mathrm{O}_2$ decreases (i.e., from ΔFMQ + 1 to ΔFMQ − 1; Fig. 3C). These values are smaller than sulfur ones, accounting for 10 to 30% of the fluid RB at ΔFMQ + 1 and from 50 to 30% of fluid RB at FMQ (fig. S6, A and B). Conversely, at ΔFMQ − 1, the low RB of sulfur means that carbon accounts for more than 92% of the total fluid RB (fig. S6C). These estimates result in metacarbonate sediment's COHS fluids with an overall oxidizing RB of +7.91, +8.44, and + 3.17 e^- mol/kg$_{\text{fluid}}$, at ΔFMQ + 1, FMQ, and ΔFMQ − 1, respectively (Fig. 3E).

We note that in the case of a carbonate-pyrrhotite–bearing mantle, the redox capacity of modeled COHS fluids will be different. At 730°C and 4.3 GPa, dissolved sulfur RB remains unchanged relative to the RB calculated using the diamond-pyrrhotite mantle reference frame (i.e., +5.4, +5.7, and +0.2 e^- mol/kg$_{\text{fluid}}$ from ΔFMQ + 1 to ΔFMQ − 1), but that of carbon is lower: −0.01 to −0.12 e^- mol/kg$_{\text{fluid}}$ (from ΔFMQ + 1 to ΔFMQ − 1; Fig. 3D). Overall, in such a scenario, modeled metacarbonate sediment's COHS fluids will retain an oxidizing RB of +5.48, +5.6, and +0.10 e^- mol/kg$_{\text{fluid}}$ from ΔFMQ + 1 to FMQ to ΔFMQ − 1, respectively (Fig. 3F). Sulfur accounts for >99% of high total fluid RB at ΔFMQ + 1 and at FMQ, while at ΔFMQ – 1, it accounts for 40 to 60% of the relatively low total fluid RB (fig. S6, D to F).

Metacarbonate-buffered slab sulfur oxidation

Current estimates for total sulfur flux from a downgoing slab are 47 to 90 million tons (Mt)/year, of which 36 to 70 Mt/year are attributed to subducted serpentinites and AOC (*24*, *48*). From our calculations, metacarbonate sediment–derived fluids, using the fluid composition modeled at 4.3 GPa and 730°C for $f\mathrm{O}_2$ at FMQ, are roughly capable of a potential S flux to the mantle wedge of just $0.22^{+2.17}_{-0.01}$ Mt/year (see Materials and Methods for details on the calculation). From such a low value, it is apparent that most sulfur entering the subarc mantle has to be delivered by S-bearing fluids rising from the entire subducting slab lithologies. These fluids can quickly flow through fracture networks or slowly permeate and

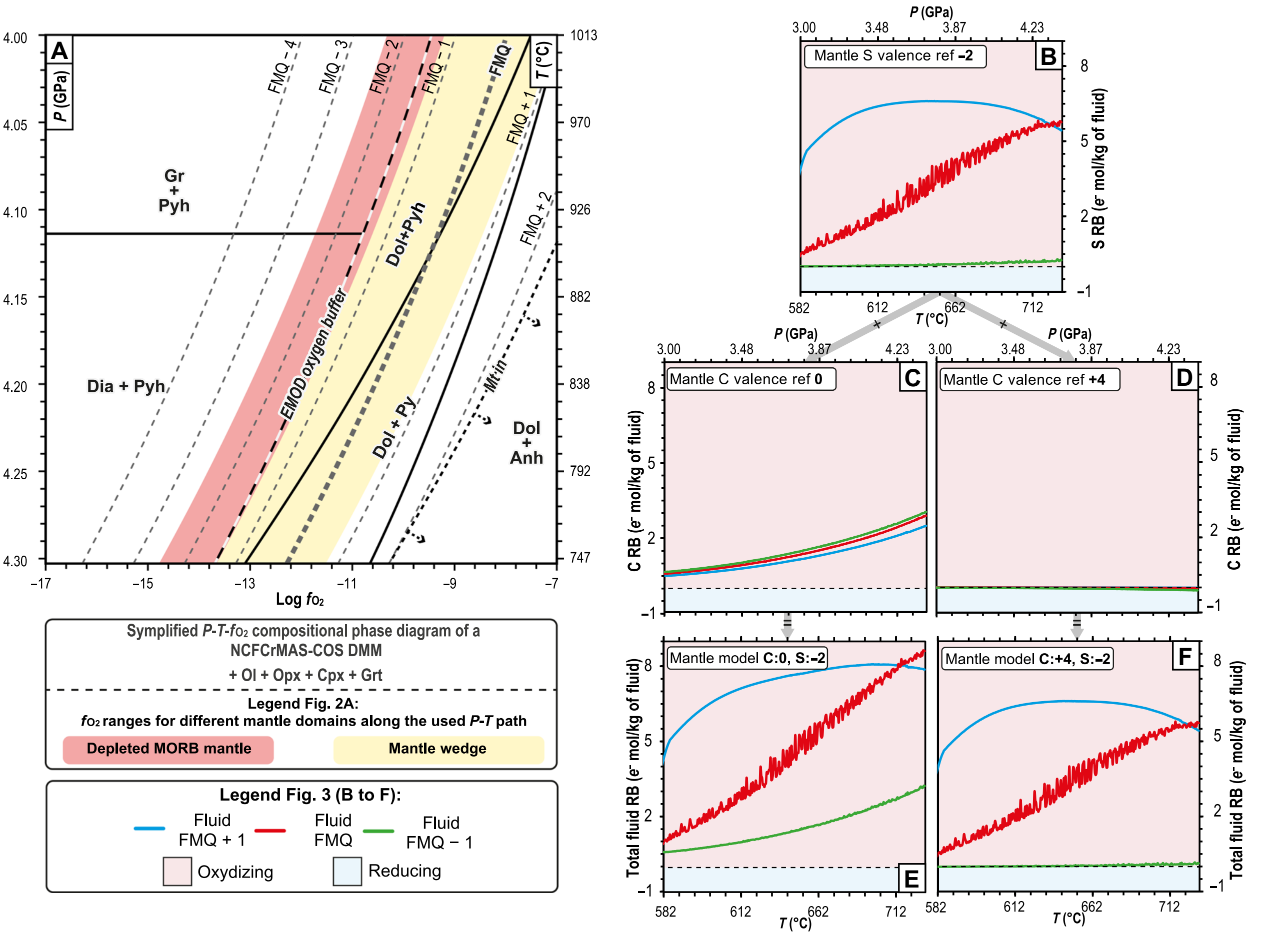

Fig. 3. Mantle P-T-fo_2 phase diagram section at the base of the wedge and fluid RB. (**A**) For simplicity, only redox-sensitive mineral phase fields relevant to C and S are indicated. The colored fields represent the fo_2 ranges for the suboceanic mantle and mantle wedge that are derived from the compilation in fig. S1 and corrected for pressure along the P-T conditions used to calculate the phase diagram (dark green line in Fig. 1A) (*66*). (**B**) S RB for a mantle in which sulfur is stable as monosulfide. (**C** and **D**) C RB for a mantle where carbon is stable as Dia/Gr or carbonate, respectively. (**E** and **F**) Total fluid RB obtained from the combination of sulfur and the two models of carbon RB (the contribution to the RB of O, H, and Fe is included but not shown here because of their extremely low contribution; see figs. S5 and S6, G to N).

reequilibrate with subducted sediments before entering the subarc mantle (*34*, *36*, *49*).

Therefore, we modeled the sulfur speciation of external S-bearing fluid infiltrating metacarbonate sediments in an open system (see Materials and Methods for details on the calculations). The starting fluid composition of S-bearing infiltrating fluids released by serpentinites and AOC at subarc depths has been modeled at 4.3 GPa and 730°C. At these conditions, serpentinite-derived fluid fo_2 range from ΔFMQ − 4.0 to ΔFMQ + 5.0 [see the recent review of (*17*)], while AOC-derived fluids can range between FMQ and ΔFMQ + 4.0 [e.g., (*50*, *51*)]. Consequently, we use a serpentinite-derived fluid composition at the FMQ and an AOC-derived fluid composition at ΔFMQ + 1.0 as infiltrating fluids. Modeled fluids show a sulfur speciation pattern, in the presence of pyrite similar to that modeled in the metacarbonate system, but with lower concentrations (i.e., Fig. 4). In serpentinites, pyrite is present above ΔFMQ − 1.5 and is completely dissolved at ΔFMQ + 0.8. At the FMQ conditions, dissolved sulfur is 0.01 mol %, and its speciation is characterized by 70% sulfate and sulfite species and only 30% of sulfide species (i.e., 0.012, 0.009, and 0.008 mol %, respectively). Hence, the dissolved S AVS is +3.1 (Fig. 4A). In the AOC, pyrite is present above ΔFMQ − 3.0 and is completely dissolved at ΔFMQ + 1.2. At ΔFMQ + 1.0, dissolved sulfur is 0.23 mol %, speciated chiefly as oxidized sulfates and sulfites and minor sulfides (0.51, 0.18, and 0.006 mol %, respectively). Hence, the dissolved S AVS is +5.4 (Fig. 4B).

We set the infiltrated metacarbonate at the FMQ, and infiltration was computed at fixed P-T (i.e., 4.3 GPa and 730°C) for the considered slab lithologies. Serpentinite-derived fluids results, on infiltration, induce metacarbonate desulfurization by pyrite dissolution (see fig. S7, A to C, for complete calculation results). On mixing with the internally derived fluid, in the presence of pyrite, dissolved sulfur speciation is dominated by sulfide species, progressively decreasing from 0.54 to 0.30 mol % (Fig. 5A). However, once pyrite is exhausted, sulfur speciation is buffered by the metacarbonate mineral assemblage. Reacted fluid composition stabilizes after roughly 400 mol of fluid react with 1 m^3 of metacarbonate. Metacarbonate-buffered serpentinite fluid has sulfates dominating sulfur fluid speciation (~0.02 mol %), with only traces of dissolved sulfites and sulfides species (0.006 and 0.003 mol %, respectively; Fig. 5A). The reacted fluid has slightly higher fo_2 (ΔFMQ + 0.24) and a higher sulfur AVS of +4.8 (Fig. 5A). Metacarbonate-buffered serpentinite fluids are oxidizing, both relative to a diamond-pyrrhotite–bearing

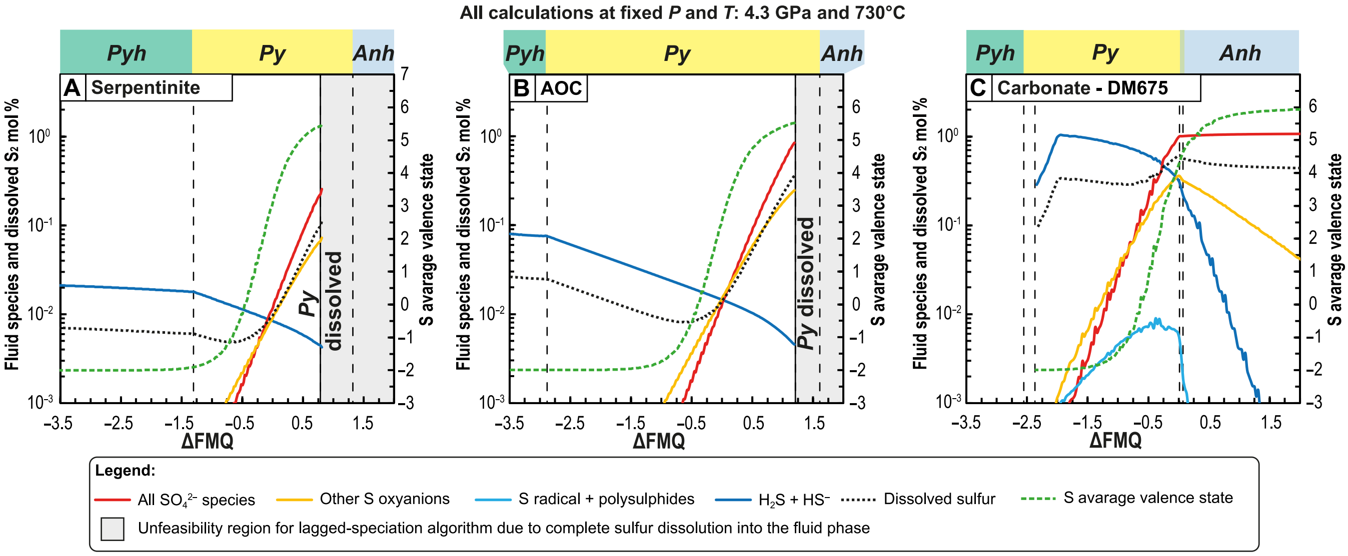

Fig. 4. Dissolved sulfur chemistry and stable sulfur mineral phases at 4.3 GPa and 730°C and as a function of fo_2 for representative subducted lithologies. Shown are the calculated sulfur speciation, total dissolved sulfur, and sulfur AVS in a fluid in equilibrium with (**A**) a representative serpentinite, (**B**) the AOC, and (**C**) the reference metacarbonate DM675. The stable mineral assemblage and the corresponding phase diagrams for serpentinite, AOC, and DM675 are reported in fig. S3. Unfeaseability regions in (A) and (B) are due to the complete dissolution of sulfur into the fluid phase, making data on modeled fluid composition at these conditions potentially unconstrained from a mass-balance point of view. Anhydrite stability is shown as a reference and has been calculated by suppressing mineral dissolution during modeling.

mantle (RB = +2.2 e^- mol/kg$_{\text{fluid}}$) and relative to a carbonate-pyrrhotite–bearing mantle (RB = +~0.1 e^- mol/kg$_{\text{fluid}}$).

The AOC-derived fluid does not lead to metacarbonate desulfurization on infiltration: Pyrite remains stable because of the high dissolved S content (see fig. S7, D to F, for complete calculation results). The fluid chemistry stabilizes after mixing with the internally derived metacarbonate fluid after ~700 mol. The reacted AOC-derived metacarbonate-buffered dissolved sulfur speciation in fluid is dominated by sulfate species (~0.75 mol %), with lower sulfite (~0.17 mol %), and by sulfide species (0.014 mol %). The reacted fluid has higher fo_2 (ΔFMQ + 0.75) and a higher sulfur AVS of +5.7 (Fig. 5A). Metacarbonate-buffered AOC fluids are oxidizing, both relative to a diamond-pyrrhotite–bearing mantle (RB = +7.1e^- mol/kg$_{\text{fluid}}$) and relative to a carbonate-pyrrhotite–bearing mantle (RB = ~+3.3 e^- mol/kg$_{\text{fluid}}$).

We note that sulfur disproportionation to oxidized species is enhanced in ultramafic and, to a lesser extent, in mafic rock compositions on equilibration with metasediments (Figs. 4 and 5). In metacarbonate-buffered slab fluids, the final dissolved sulfate concentration increases by 50 to 70% higher than in the initial serpentinite-and AOC-derived fluids. In addition, in reequilibrated fluids, carbon speciation is dominated by bicarbonate and carbonate ions (fig. S7, B and E). These results show that C and S in serpentinite- and AOC-derived fluids are reset predominantly to oxidized species on infiltration. Metacarbonate sediments act as oxidative filters (*34*) on pyrite disproportionation, releasing oxidizing species into the subarc mantle.

DISCUSSION

Carbon-to-sulfur redox handover at convergent margins

Geodynamics at convergent margins governs Earth's volatile cycling from the surface to the mantle and back. Slab rocks' pressure, temperature, and fo_2 conditions are critical to the capacity for mass transport of subduction fluids to the overlying mantle wedge. During deep subduction (100 to 200 km), mineral dissolution can release a considerable fraction of carbon and sulfur due to increased solubility in aqueous fluids at increasing temperatures. Fluid inclusions in pyrite-bearing metasediments from Lago di Cignana (Western Alps) provide robust direct evidence for the presence of dissolved SO_4^{2-} complexes, along with carbonate and bicarbonate ions, in aqueous fluids released at about 110 km in depth during deep subduction [e.g., (*20*, *27*, *28*)].

The oxidative capacity of subduction zone fluids is determined by a subduction-specific combination of several interplaying factors: (i) subducted rocks and released fluids' redox state, (ii) the available fluid mass and flux (i.e., dehydration reaction rate), (iii) the availability of soluble redox-sensitive elements, and (iv) redox condition of mantle wedge rocks. Given the widespread occurrence of subducted sediment signatures in arc magmatism (*52*), believed to result from the influence of sediment-buffered slab fluids, it is reasonable to assume that fluid transport in the uppermost section of a subducting slab at subarc depths occurs by porous flow. Such a process, as also shown here, is fully capable of resetting serpentinite-derived and AOC-derived fluid chemistry to that of the sediment layer within a few meters of infiltration (*34*, *36*).

The oxidation potential of metacarbonate-buffered COHS slab fluids can thus be evaluated by estimating the time necessary (i.e., the efficiency) to oxidize the subarc mantle by fluids released by all slab lithologies, starting from a DMM (see Materials and Methods). Initiation of arc magmatism, marking the first effect of subduction fluids on the mantle wedge, occurs within 1 to 33 million years (Myr) (clustering at 7 Myr) from subduction initiation (*10*, *52*, *53*), signaling the arrival of the slab at subarc depths. Composite COHS fluids derived by combining a serpentinite-derived and AOC-derived fluid buffered by metacarbonate sediments and the internally derived metacarbonate sediment fluid have been mass-balanced with H_2O

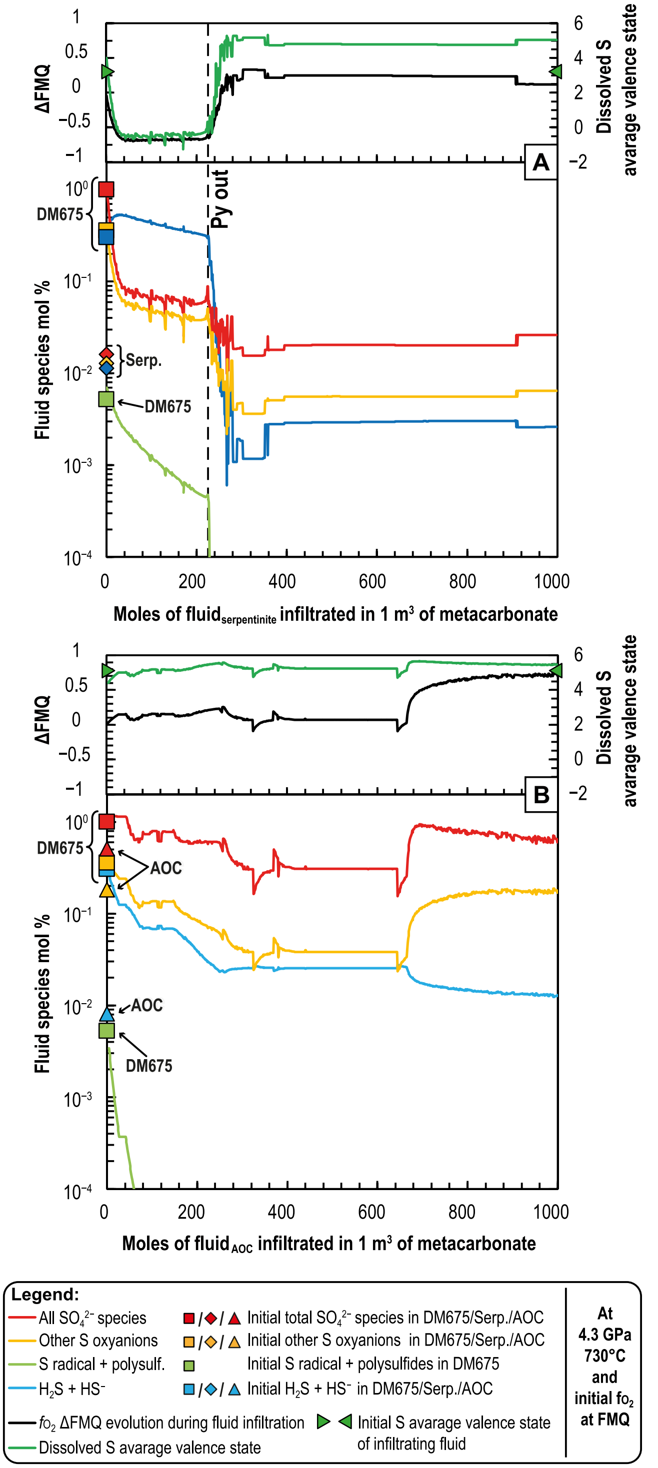

Fig. 5. Oxidation of dissolved sulfur in serpentinite-derived and AOC-derived fluids infiltrating 1 m^3 of metacarbonate rocks at subarc depths. (**A**) Reported fluid data for a serpentinite-derived fluid infiltrating and reequilibrating with reference metacarbonate DM675. (**B**) Reported fluid data for an AOC-derived fluid infiltrating and reequilibrating with reference metacarbonate DM675. The changes to other fluid species, to the stable mineral phases, and to the fluid RB for both scenarios are reported in fig. S7.

fluxes from downgoing slabs globally, which greatly vary from 180 to 800 Mt/year of H_2O (see Materials and Methods for details) (*54*). At these conditions, the subarc mantle can be oxidized to the carbonate stability field (i.e., to the EMOD buffer) within 0.23 to 1.00 Myr after subduction initiation, depending on the H_2O flux at subarc depths (Figs. 6 and 7). For an averaged slab fluid flux of 490 Mt/year of H_2O, metacarbonate-buffered COHS slab fluids (i.e., dominated by C^{4+} and $S^{6+} \pm S^{4+}$ species) will oxidize the subarc mantle within 2.3 to 8 Myr to average fo_2 values of ΔFMQ − 0.65 to ΔFMQ + 0.85 (i.e., that of the deep subarc mantle) (*55*). Obtained timing indicates wedge oxidation as a fast process, matching the timeframe of the beginning of arc magmatism. Higher or lower fluid fluxes result in 1.4 to 4.7 Myr to 6 to 21 Myr of time required to oxidize the subarc mantle, respectively (Figs. 6 and 7). Such a range of values can reflect differences in slab fluid production rate, slab geometries—and consequently, the volume of mantle wedge to be affected—and porosity-dependent fluid transfer rate through the downgoing slab and the subarc mantle. For example, 10 Myr after subduction initiation, the subarc mantle redox state can span ~2.5 log fo_2 units solely due to different fluid influxes into the mantle wedge. Critically, such a value matches the spread observed in subarc mantle xenoliths (i.e., ~2.5 log fo_2 units; fig. S1B). High oxidation rates, in the order of ≪5 Myr, by short-timescale fluid-mediated slab component addition (from <0.01 to 0.15 Myr) to the arc magma generation region, are also suggested by ^{238}U-^{230}Th, ^{235}U-^{231}Pa and ^{226}Ra-^{230}Th disequilibrium in arc lavas [e.g., (*56, 57*)].

Such a fast oxidation rate of the mantle wedge driven by slab-derived COHS fluids appears to be substantially influenced by dissolved oxidized sulfur, which assumes that sufficient sulfur is present in the subducting slab. As an example (see Supplementary Text for a detailed explanation of this mass-balance constraint), a mass-balance calculation can be based on the AOC as the primary source (71% of total sulfur influx) (*24*). Our modeling shows that 1 m^3 of AOC containing 0.06 mol % of pyrite at 4.3 GPa, 730°C, and ΔFMQ + 1 releases 22,878 mol of fluid, of which 51.95 mol are of sulfur with an AVS of +5.41. At 4.27 GPa and 780°C, in 1 m^3 of overlying DMM with an average fo_2 of −1.94 Δlog units, the oxidation of 38.54 mol of Fe^{2+} to Fe^{3+} is necessary to match the oxidized mantle wedge's conditions. Upon reduction during mantle wedge oxidation, the dissolved sulfur in the AOC-derived fluid can oxidize 7.41 mol of Fe^{2+} to Fe^{3+}, providing an oxidative capacity to oxidize 384.84 mol of Fe^{2+}. This is sufficient to increase the redox state by ~2 log fo_2 units in 6.3 m^3 of DMM. The presented values are yet another way to showcase the high oxidative capacity of sulfur-bearing fluids.

In the mantle wedge, most peridotites lie below the EMOD buffer, and at these conditions, the reduction of carbonates in aqueous fluids to diamond or graphite, depending on pressure, will increase mantle fo_2 [e.g. (*47, 58*)]. Our modeling shows, however, that sulfur in fluids released by sulfide mineral dissolution bears the most oxidative capacity due to disproportionation as sulfate, sulfite, and sulfide species. Sulfur disproportionation in fluids is a crucial process that enables reduced subarc subducting rocks to acquire an unexpected oxidative capacity that is then transferred to the mantle wedge by released fluids.

Carbon and sulfur promote mantle wedge oxidation. Complex COHS fluids, carrying oxidized carbon (C^{4+}) and sulfur ($S^{6+} \pm S^{4+}$) in different proportions, have a high oxidative capacity, potentially increasing mantle fo_2 above the EMOD buffer very shortly from

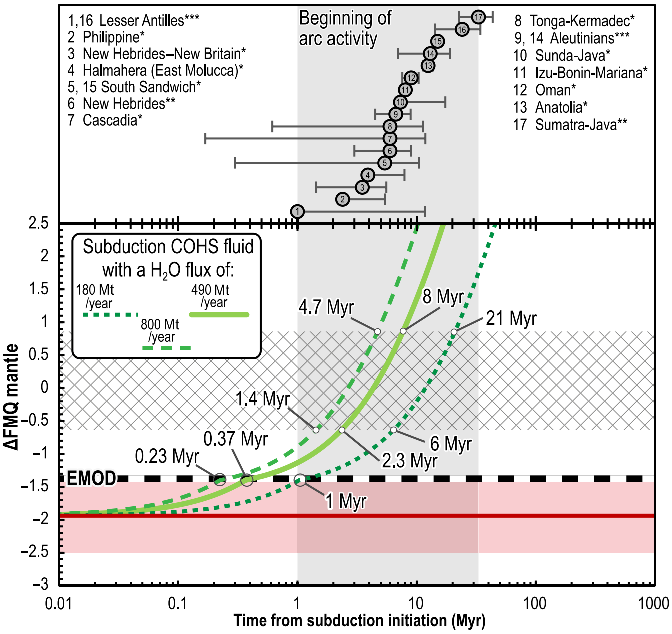

Fig. 6. Time-fo_2 evolution for a DMM mantle by interaction with COHS fluids metacarbonate-buffered slab fluids as a function of H_2O flux to the subarc mantle. The time span intercurred between subduction initiation and arc magmatism onset for subduction zones that have been active during the Cenozoic and the Late Cretaceous is taken from (*53, 81*). *Data from (*53*). **Data from (*81*). ***Two ages for the same subduction zone from (*53*) and (*81*).

subduction initiation (<1 Myr; Fig. 7). At fo_2 values above this reaction, carbonates and CO_2 will be present in peridotites, considerably reducing aqueous carbon oxidizing capacity. Consequently, further increase in mantle wedge redox state to FMQ and ΔFMQ + 1 values requires the reduction of S^{+6} and S^{4+} in fluids.The overall mantle wedge oxidation process at arc magma genesis depth depends on the H_2O flux and, thus, the *P-T* conditions at which the dehydration reactions initiate. Cold subduction zones are more likely to be characterized by high fluid fluxes (*54*), thus reaching the condition of a fully oxidized mantle wedge (i.e., by increasing fo_2 of ~3 log units) faster than hot ones (i.e., <5 Myr) (*59*). Whatever the case, the modeled oxidation rate suggests that the subarc mantle is fully oxidized over the entire duration of the arc magmatic activity. Mantle wedge oxidation shortly after subduction onset profoundly influences the cycling of redox-sensitive elements, the overall mass transport of trace elements, and the nature of volcanic gasses (e.g., CO_2 and SO_2), ensuring continuity in deep volatile cycles, further promoting the planet's habitability.

MATERIALS AND METHODS

Thermodynamic modeling (models construction and assumptions)

All phase equilibrium calculations were performed by free energy minimization using Perple_X (version 6.9.1, last accessed 2 December 2022, for all calculations except "0-dimensional (0D) infiltration," for which 7.1.1., last accessed 13 July 2023, due to better troubleshooting capabilities) (*60*). All the rock bulk and infiltrating fluid compositions used in all the below thermodynamic calculations are reported in table S2. The condensed phase and molecular volatile species data from (*61*) (revised 2018, version DS6.22) and solute species data from the DEW/HKF model of (*62*) (revised 2017) have been used. The properties of H_2O, CO_2, CH_4, H_2S, and C_2H_6 were described using the solvent reference state, whereas, because of their negligible abundance, CO and SO_2 were described relative to the solute reference state. The equation of state of (*63*) was used to compute the properties of pure H_2O and CO_2, and the modified Redlich-Kwong equation of state of (*64*) was used to compute the properties of all other solvent species and the activities of all solvent species. For the carbonate sediment composition [Ca-Mg-Fe-Si-C-O_2-H_2-S_2, CMFS-COHS system; DM675; for details on the composition, see (*39*, *40*)], the closed system phase equilibria were calculated with the "Lagged Speciation" algorithm (an iterative version of the back-calculation algorithm) (*60, 65*). The solid solution models used for the chemical phase diagram calculations for DM675 are reported in table S6.

The DM675 *T*(*P*)-fo_2 chemical phase diagram (Fig. 1B and fig. S3) has been calculated along the prograde Brossasco-Isasca Unit (BIU; major UH*P* unit of the Dora-Maira Massif) *P-T* path by calculating two different but contiguous phase diagrams with the use of two different polynomial equations (table S1). For the *T*(*P*)-fo_2 mantle phase diagrams (Fig. 3A), the composition of the DMM from (*46*) has been used. The solid solution models used for DMM's chemical phase diagram calculations are reported in table S6. The calculations have been performed along the potential *P-T* path of the fluid ascent from the slab into the deeper portion of the mantle wedge (*66*).

The sulfur speciation data shown in Fig. 4 have been calculated as closed system chemical phase diagrams (using Lagged Speciation algorithm) in a restricted *P-T*-fo_2 range (727° to 731°C; $-10 < fo_2 < -16$; fig. S3), along the same *P-T* path used for the DM675 *T*(*P*)-fo_2 chemical phase diagram (Fig. 1B and fig. S3). The calculated speciation, for straightforward comparison with that of DM675, has been evaluated at fixed *P-T* conditions (730°C and 4.3 GPa) and in a fo_2 range between ΔFMQ − 3.5 and ΔFMQ + 2.0. The lithotypes for which the calculations have been performed are the major ones being currently subducted:

1) Serpentinite, Ca-S–bearing [S: 641 parts per million (ppm)] and hydrated KLB-1 composition [from (*67*)] modified following (*17*).

2) AOC, using the Honshu bulk composition (S: 850 ppm) from (*14*).

The solid solution models used for the chemical phase diagram calculations for serpentinite and AOC are reported in table S6. The additional (relative to the DM675 calculations) stable pure phases are lawsonite and coesite.

Open-system "0D infiltration" calculations have been performed to test what might be the nature of fluids rising from within the slab (chiefly from the serpentinised mantle and from the AOC) after having interacted with 1 m^3 of DM675-like metacarbonate sediment sitting atop the subducting pile. Here, the limit case of pure porous flow has been modeled. In this way, the maximum reequilibration between the infiltrating external fluids and the metacarbonate is guaranteed. Modeling has been performed in steps of 1 mol of fluid aliquot infiltrating and subsequently fractionating the system 1000 times, meaning that at the end of the calculations, 1000 mol of fluids have infiltrated 1 m^3 of DM675-like metacarbonate sediment. The fluid has been fractionated in such a way that the fluid porosity would be <1 vol %, which is a reasonably low value that still allows simulating an effective fluid porosity within a slab at subarc depths

(0.01 to 4 vol %) as derived from petrologic studies [e.g., (*68*)]. The solid solution models used for the 0D infiltration calculations are reported in table S6. No additional pure phase has been predicted.

Fluids are generally thought to be released as soon as they are produced and reach a critical volume fraction sufficient to form either an interconnected porous flow or to coalesce into a vein system. However, the results and calculations presented here have been conducted in a closed system along the entire prograde *P-T* path. This is justified when UH*P* peak fluid inclusion composition has been reproduced by thermodynamic modeling simulating closed system behavior [compare (*39*)]. Moreover, as shown in magnetotelluric imaging (*69*) and thermomechanical modeling (*70*), the bulk of subduction-zone fluids is likely to escape the slab at subarc depths, thus requiring a mostly closed system behavior at least until subarc depths are reached. The composition of all fluids rising through the slab will be reset in the thin dissolving sedimentary layer sitting atop the subducting plate within a few meters upon arrival in the sediment column (*36*). Similarly, the slab's fluid oxidizing capacity, necessary to oxidize the subarc mantle, is imposed by the sediment's redox-sensitive mineral assemblage (*34*). This was further tested by performing open-system 0D infiltration calculations, confirming these observations.

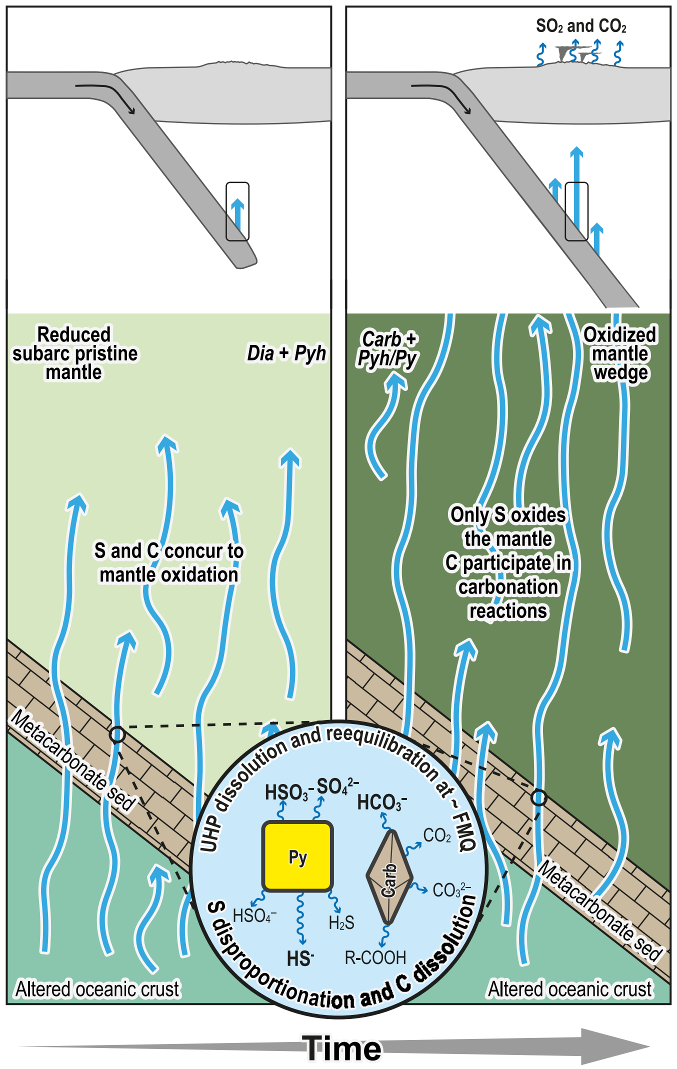

Fig. 7. Schematic illustration of the presented model (not to scale). Solute-bearing aqueous COHS equilibrated with subducted metacarbonates sediments, in which carbonates are dissolving, and pyrite is disproportioning into the fluid, rising through the base of the subarc mantle, oxidizing it over time. Hence, COHS fluids oxidize the mantle wedge to the point of stabilizing carbonates (i.e., reaching the EMOD buffer), C loses its oxidizing capacity (it only carbonates the mantle), and only S can further increase mantle wedge fo_2.

Given the complete lack of information regarding the sediment's fo_2 evolution at subarc depths [only existing information is for particularly oxidized sediments equilibrated at forearc conditions (*34*) and for some marbles (*71*), at $P < 1.5$ GPa], the thermodynamic model has been explored along profiles at fixed fo_2. Nevertheless, the explored fo_2 range is compatible with what can be reasonably expected in sediment at subarc depth by applying the same change of fo_2, with increasing depth, observed for the mantle: a decrease of 0.5 log fo_2 per 1 GPa of pressure increase. Starting from the clustering in fo_2 estimates for sediments, especially marbles, reported by (*34*), around ΔFMQ + 2.5 at 1.5 and 3.5 GPa, sediments might be at ΔFMQ + 1.5, and 4.5 GPa might be at ΔFMQ + 0.5.

Average valence state

The AVS of an element E (both in the rock assemblage and the fluid), characterized by *n* possible valence state values, has been calculated as the weighted average

$$\text{AVS E} = \frac{\text{moles E}^{\text{VS}_1} \cdot \text{VS}_1 + \text{moles E}^{\text{VS}_2} \cdot \text{VS}_2 + \ \dots \ + \text{moles E}^{\text{VS}_n} \cdot \text{VS}_n}{\sum \text{moles E}}$$

Where VS_i is the value of the valence states that can be acquired by element E (e.g., for C, $-4 < \text{VS}_i < +4$), E^{VS_i} are the moles of element E with the valence state VS_i. The data necessary for each species are reported in table S4 and S5.

Redox budget

The RB (*43*) is an extensive variable describing a geologic system's oxidizing/reducing capacity and is determined by the quantity of redox-sensitive elements present and their valence state. It is calculated on the basis of the number of moles of electrons that need to be added to a geologic system to reach a predetermined redox reference state

$$\text{RB} = \sum_i n_i v_i$$

$$v_i = (v_{\text{sample}} - v_{\text{reference}})$$

where n_i is the number of moles of redox-sensitive element *i* and v_i is the number of electrons required to take one mole of element *i* at a specific initial valence state to the reference valence state. Here, we calculated the RB of fluids by determining the valence state of each redox-sensitive element in each species present in the fluid, and from there, the abundance of the redox-sensitive elements in all their possible valence state was calculated. This has been used to calculate the AVS of element *i*, which is the value used to calculate the difference between the reference valence state (in the mantle) and the fluid valence state. To better quantify redox fluxes, the RB has been dimensioned as a specific quantity, i.e., as a specific RB (e^- mol/kg_{fluid}) (*44*), following the below conversion passages

$$\boldsymbol{E}(\mathrm{mol}) \cdot \textbf{molar weight}\, \boldsymbol{E}\left(\frac{\mathrm{g}}{\mathrm{mol}}\right) = \boldsymbol{E}(\mathrm{g})$$

$$\left[\frac{\boldsymbol{E}(\mathrm{g})}{\sum \boldsymbol{E}_{\mathbf{fluid}}(\mathrm{g})}\right] \cdot 1000 = \boldsymbol{E}\left(\frac{\mathrm{g}}{\mathrm{kg}_{\mathrm{fluid}}}\right)$$

$$\boldsymbol{E}\left(\frac{\mathrm{g}}{\mathrm{kg}_{\mathrm{fluid}}}\right) \textbf{molar weight}\; \boldsymbol{E}\left(\frac{\mathrm{g}}{\mathrm{mol}}\right) = \boldsymbol{E}\left(\frac{\mathrm{mol}}{\mathrm{kg}_{\mathrm{fluid}}}\right)$$

$$\boldsymbol{E}\left(\frac{\mathrm{mol}}{\mathrm{kg}_{\mathrm{fluid}}}\right) \cdot (\boldsymbol{v}_{\mathbf{sample}} - \boldsymbol{v}_{\mathbf{reference}}) = \mathbf{RB}\left(\frac{e^{-}\mathrm{mol}}{\mathrm{kg}_{\mathrm{fluid}}}\right)$$

Sulfur RB has been calculated for atomic S and not diatomic S_2.

Calculation of mantle oxidation evolution over time

To test whether the modeled fluids and associated RB are to be compared with observed oxygen fugacities, a relation correlating them is necessary. Evans and Tomkins (*72*) and Evans (*43*) have proposed multiple arbitrary functions relating the $f\mathrm{O}_2$ and the specific RB of a C-free but with a combination of H_2O-bearing or S-bearing (with different concentrations) depleted subarc mantle compositions (DMM) (*46*) at 1200°C and 1 GPa. As (*72*) pointed out, different mantle compositions at different *P-T* conditions will be characterized by different buffering capacities. Nevertheless, these calculations must be based on simplifying assumptions, with significant errors arising from using average values and a simplistic model. Thus, the obtained data must be considered semiquantitative at best.

Two relations between mantle $f\mathrm{O}_2$ and specific RB have been calculated for the mantle modeled in Fig. 3A: a DMM (*46*) with 119 ppm of S and with 52 ppm of C [upper value of (*73*) due to changing concentration with depth of (*74*)]. The increase in Fe^{3+} as mantle's $f\mathrm{O}_2$ increase has been calculated at fixed *P-T* (4.27 GPa and 780°C). Since, in the calculated model, diamond is oxidized to dolomite (i.e., EMOD oxygen buffer) (*47*) at roughly ΔFMQ − 1.4, the specific RB necessary to oxidize such a mantle suddenly increases at this reaction. This means a single and continuous function relating $f\mathrm{O}_2$ and RB could not be derived. Thus, one function has been fitted for a diamond-bearing mantle and one for a carbonate-bearing mantle. In Fig. 3A it is also shown that pyrrhotite is substituted by pyrite at roughly ΔFMQ − 0.65. However, such a reaction translates to a 10^{-5} change to the mantle's specific RB. Moreover, the pyrite field in Fig. 3A appears to close outside the modeled *P-T* range. For these reasons, the transition to a pyrite-bearing from a pyrrhotite-bearing mantle has been ignored since the error introduced is negligible. Following (*43*) and (*72*), the chosen functions, although arbitrary, are the simplest ones capable of replicating the mantle $f\mathrm{O}_2$-specific RB relationships (fig. S8)

$$\Delta\mathrm{FMQ}_{\mathrm{DMM}_{\mathrm{Dia}}} = 6.65310538 + 1.92522872 \cdot \ln(\mathrm{RB}_{\mathrm{DMMDia}}) \quad (1)$$

$$\Delta\mathrm{FMQ}_{\mathrm{DMM}_{\mathrm{Dol}}} = 10.92384084 + 3.56279812 \cdot \ln(\mathrm{RB}_{\mathrm{DMMDol}}) \quad (2)$$

Because of the discontinuous nature of Eqs. 1 and 2, as shown in fig. S8, once the calculation for $\Delta\mathrm{FMQ}_{\mathrm{DMMDia}}$ reached the EMOD, it is necessary to switch to Eq. 2. However, it is necessary to add, to the result obtained by Eq. 2, the difference in ΔFMQ between the last value obtained by Eq. 1 and the first value obtained from Eq. 2 and then recalculate. This is needed to avoid an apparent reduction of the mantle due to the topology of the two equations. In Eqs. 1 and 2, $\mathrm{RB}_{\mathrm{DMMDia}}$ is calculated as

$$\mathrm{RB}_{\mathrm{DMMDia}} = \mathrm{RB}_{\mathrm{DMM}_{\mathrm{Dia}}}^{\mathrm{initial}} + \frac{\mathrm{Global\ RB}_{\mathrm{Fluid}}^{\mathrm{DMM}_{\mathrm{Dia}}} \cdot t}{M_{\mathrm{M}} \cdot f} \quad (3)$$

while $\mathrm{RB}_{\mathrm{DMMDol}}$ is calculated as

$$\mathrm{RB}_{\mathrm{DMMDol}} = \mathrm{RB}_{\mathrm{DMM}_{\mathrm{Dol}}}^{\mathrm{initial}} + \frac{\mathrm{Global\ RB}_{\mathrm{Fluid}}^{\mathrm{DMM}_{\mathrm{Dol}}} \cdot t}{M_{\mathrm{M}} \cdot f} \quad (4)$$

Here, M_{M} is the mass of the mantle (3.64×10^{24} kg), *t* is time in years, $\mathrm{RB}_{\mathrm{DMM}_{\mathrm{Dia}}}^{\mathrm{initial}}$ and $\mathrm{RB}_{\mathrm{DMM}_{\mathrm{Dol}}}^{\mathrm{initial}}$ are the specific mantle RB calculated at the average $f\mathrm{O}_2$ of the DMM and EMOD buffer, respectively. *f* is the proportion (i.e., volume) of the affected subarc mantle. Assuming (in a lithostatic configuration) an arc crust of 30 km in thickness (with a density of 2750 kg/m^3), modeled fluids enter the subarc mantle at a depth of ~139 km and interact with the mantle up to 2.2 GPa (i.e., up to ~72 km in depth assuming a mantle density of 3369.7 kg/m^3,value derived from the calculated model and used for consistency). This pressure value has been chosen as an average value due to carbonates undergoing decarbonation reactions in the mantle at 2.6 to 1.8 GPa and between 1000° and 1400°C [e.g., (*75*), and references therein]. Given a trench-to-arc distance of ~97 km and a 55° slab dip, the final volume of mantle considered to be effectively interacting with slab fluids is 67 km in depth ($\mathrm{Subd}_{\mathrm{Depth}}$), 47 km in width ($\mathrm{Subd}_{\mathrm{Arc}}$; i.e., horizontal distance, at 72 km in depth, between the slab and the vertical line connecting the volcanic arc and the location of fluid escape from the slab modeled here), and 44,450 km in length ($\mathrm{Subd}_{\mathrm{Length}}$; global horizontal slab length) (*76*). Thus

$$f = \frac{M_{\mathrm{M}}}{\mathrm{Subd}_{\mathrm{Length}} \cdot \mathrm{Subd}_{\mathrm{Depth}} \cdot \mathrm{Subd}_{\mathrm{Arc}} \cdot 0.5 \cdot 10^{9*} \rho_{\mathrm{M}}} = 0.00064 \quad (5)$$

Last, $\mathrm{Global\ RB}_{\mathrm{Fluid}}^{\mathrm{Mantle}_{\mathrm{Dia}}}$ and $\mathrm{Global\ RB}_{\mathrm{Fluid}}^{\mathrm{Mantle}_{\mathrm{Dol}}}$ are the specific fluid RB (expressed as e^{-} mol/$\mathrm{kg}_{\mathrm{fluid}}$), relative to a diamond-bearing and a dolomite-bearing mantle. They have been obtained by mass balancing the corresponding specific RB of serpentinite-derived and AOC-derived fluids after equilibration with 1 m^3 of metacarbonate sediments (Fig. 5 and fig. S7). These fluids have been scaled such that serpentinite-derived and AOC-derived fluids constitute 48 and 43% of the total fluid flux at subarc depth (*70*), respectively. The remaining 9% will be represented by metacarbonate-derived fluid calculated at the FMQ buffer (Fig. 2, E and F) Such a composite fluid composition has been further mass-balanced with the global H_2O flux produced by global subductions between 100 and 150 km [1.8×10^{11} to 8.0×10^{11} kg/year; estimated by (*54*)]. Assuming that all subduction zone fluids are fully chemically reset by interacting with the subducted sediments before entering the subarc mantle (*34*, *36*), the H_2O flux has been assumed to be entirely equilibrated with a sediment column composed solely of metacarbonate sediments. Overall, these calculations allow for the drawing of a relation between the time it takes for a fluid with a specific redox capacity to oxidize the subarc mantle from a starting $f\mathrm{O}_2$ value to a desired one. In the presented model, the starting value is the average $f\mathrm{O}_2$ of a reduced DMM (i.e., ΔFMQ − 1.94) at depth.

Mass-balance calculations

Evaluation of the potential dissolved S flux from subducted metacarbonate sediments globally. The flux has been calculated as

$$\text{S Flux (Mt/year)} = \frac{M \times V_{\text{Car}} \cdot \text{S.R.} \cdot [\text{S}]_{\text{Fluid}}}{10^{-9}} = 0.221^{+2.17}_{-0.01}\ \text{S (Mt/year)}$$

where M is the mass of the calculated fluid at 730°C, 4.3 GPa, and at the FMQ buffer produced by 1 m^3 of metacarbonate sediment (55.48 kg). V_{Car} is the volume (in cubic meters) of the subducted carbonate sediments, which is given by the median carbonate proportion (42 m) (*37*) at the trench multiplied by the total length of subduction zones worldwide (44,450 km) (*76*). S.R. is the median subduction rate (0.062 m/year) from (*70*). $[\text{S}]_{\text{Fluid}}$ is the concentration of S, for the fluid modeled in equilibrium with the DM675 metacarbonate system at the above P-T-$f\text{O}_2$ conditions, as weight % (3.396 wt %).

Supplementary Materials

This PDF file includes:

Supplementary Text
Figs. S1 to S9
Tables S1 to S6

Other Supplementary Material for this manuscript includes the following:

Auxiliary References

REFERENCES AND NOTES

1. I. S. Carmichael, The redox states of basic and silicic magmas: A reflection of their source regions? *Contrib. Mineral. Petrol.* **106**, 129–141 (1991).
2. S. A. Carn, L. Clarisse, A. J. Prata, Multi-decadal satellite measurements of global volcanic degassing. *J. Volcanol. Geotherm. Res.* **311**, 99–134 (2016).
3. T. P. Fischer, S. Arellano, S. Carn, A. Aiuppa, B. Galle, P. Allard, T. Lopez, H. Shinohara, P. Kelly, C. Werner, C. Cardellini, G. Chiodini, The emissions of CO_2 and other volatiles from the world's subaerial volcanoes. *Sci. Rep.* **9**, 18716 (2019).
4. J. Lelieveld, J. Heintzenberg, Sulfate cooling effect on climate through in-cloud oxidation of anthropogenic SO_2. *Science* **258**, 117–120 (1992).
5. J. Hansen, M. K. I. Sato, R. Ruedy, L. Nazarenko, A. Lacis, G. A. Schmidt, G. Russell, I. Aleinov, M. Bauer, S. Bauer, N. Bell, B. Cairns, V. Canuto, M. Chandler, Y. Cheng, A. Del Genio, G. Faluvegi, E. Fleming, A. Friend, T. Hall, C. Jackman, M. Kelley, N. Kiang, D. Koch, J. Lean, J. Lerner, K. Lo, S. Menon, R. Miller, P. Minnis, T. Novakov, V. Oinas, J. Perlwitz, J. Perlwitz, D. Rind, A. Romanou, D. Shindell, P. Stone, S. Sun, N. Tausnev, D. Thresher, B. Wielicki, T. Wong, M. Yao, S. Zhang, Efficacy of climate forcings. *J. Geophys. Res. Atoms* **110**, 2005JD005776 (2005).
6. C. T. A. Lee, P. Luffi, V. Le Roux, R. Dasgupta, F. Albaréde, W. P. Leeman, The redox state of arc mantle using Zn/Fe systematics. *Nature* **468**, 681–685 (2010).
7. K. A. Kelley, E. Cottrell, Water and the oxidation state of subduction zone magmas. *Science* **325**, 605–607 (2009).
8. M. Brounce, K. A. Kelley, E. Cottrell, M. K. Reagan, Temporal evolution of mantle wedge oxygen fugacity during subduction initiation. *Geology* **43**, 775–778 (2015).
9. A. Bénard, K. Klimm, A. B. Woodland, R. J. Arculus, M. Wilke, R. E. Botcharnikov, N. Shimizu, O. Nebel, C. Rivard, D. A. Ionov, Oxidising agents in sub-arc mantle melts link slab devolatilisation and arc magmas. *Nat. Comm.* **9**, 3500 (2018).
10. P. Tollan, J. Hermann, Arc magmas oxidized by water dissociation and hydrogen incorporation in orthopyroxene. *Nat. Geosci.* **12**, 667–671 (2019).
11. M. J. Muth, P. J. Wallace, Slab-derived sulfate generates oxidized basaltic magmas in the southern Cascade arc (California, USA). *Geology* **49**, 1177–1181 (2021).
12. B. J. Wood, L. T. Bryndzia, K. E. Johnson, Mantle oxidation state and its relationship to tectonic environment and fluid speciation. *Science* **248**, 337–345 (1990).
13. D. J. Frost, C. A. McCammon, The redox state of Earth's mantle. *Annu. Rev. Earth Planet. Sci.* **36**, 389–420 (2008).
14. J. B. Walters, A. M. Cruz-Uribe, H. R. Marschall, Sulfur loss from subducted altered oceanic crust and implications for mantle oxidation. *Geochem. Persp. Let.* **13**, 36–41 (2020).
15. W. Y. Duan, X. P. Li, H. P. Schertl, A. P. Willner, C-O-H-S fluids released by oceanic serpentinite in subduction zones: Implications for arc-magma oxidation. *Earth Planet. Sci. Lett.* **594**, 117709 (2022).
16. Y. B. Li, Y. Chen, B. Su, Q. H. Zhang, K. H. Shi, Redox species and oxygen fugacity of slab-derived fluids: Implications for mantle oxidation and deep carbon-sulfur cycling. *Front. Earth Sci.* **10**, 974548 (2022).
17. K. A. Evans, B. R. Frost, Deserpentinization in subduction zones as a source of oxidation in arcs: A reality check. *J. Petrol.* **62**, egab016 (2021).
18. J. C. Alt, C. J. Garrido, W. C. Shanks III, A. Turchyn, J. A. Padrón-Navarta, V. L. Sánchez-Vizcaíno, M. T. G. Pugnaire, C. Marchesi, Recycling of water, carbon, and sulfur during subduction of serpentinites: A stable isotope study of Cerro del Almirez, Spain. *Earth Planet. Sci. Lett.* **327–328**, 50–60 (2012).
19. E. M. Schwarzenbach, M. J. Caddick, M. Petroff, B. C. Gill, E. H. Cooperdock, J. D. Barns, Sulphur and carbon cycling in the subduction zone mélange. *Sci. Rep.* **8**, 15517 (2018).
20. F. Giacometti, K. A. Evans, G. Rebay, J. Cliff, A. G. Tomkins, P. Rossetti, G. Vaggelli, D. T. Adams, Sulfur isotope evolution in sulfide ores from Western Alps: Assessing the influence of subduction-related metamorphism. *Geochem. Geophys. Geosystems.* **15**, 3808–3829 (2014).
21. J. B. Walters, A. M. Cruz-Uribe, H. R. Marschall, Isotopic compositions of sulfides in exhumed high-pressure terranes: Implications for sulfur cycling in subduction zones. *Geochem. Geophys. Geosystems.* **20**, 3347–3374 (2019).
22. J. L. Li, R. Klemd, G. F. Huang, J. J. Ague, J. Gao, Unravelling slab δ34S compositions from in-situ sulphide δ34S studies of high-pressure metamorphic rocks. *Int. Geol. Rev.* **63**, 109–129 (2021).
23. F. Piccoli, J. Hermann, T. Pettke, J. A. S. Connolly, E. D. Kempf, J. F. Vieira Duarte, Subducting serpentinites release reduced, not oxidized, aqueous fluids. *Sci. Rep.* **9**, 19573 (2019).
24. J. L. Li, E. M. Schwarzenbach, T. John, J. J. Ague, F. Huang, J. Gao, R. Klemd, M. J. Whitehouse, X. S. Wang, Uncovering and quantifying the subduction zone sulfur cycle from the slab perspective. *Nat. Comm.* **11**, eabj2515 (2020).
25. J. M. de Moor, T. P. Fischer, T. Plank, Constraints on the sulfur subduction cycle in Central America from sulfur isotope compositions of volcanic gases. *Chem. Geol.* **588**, 120627 (2022).
26. L. J. Xu, S. A. Liu, Uncovering the redox state and S species of subduction zone fluids from Zn isotope systematics of eclogites in Northern Qilian and Southwestern Tianshan. *Lithos* **436-437**, 106979 (2023).
27. M. L. Frezzotti, J. Selverstone, Z. D. Sharp, R. Compagnoni, Carbonate dissolution during subduction revealed by diamond-bearing rocks from the Alps. *Nat. Geosci.* **4**, 703–706 (2011).
28. M. L. Frezzotti, S. Ferrando, The chemical behavior of fluids released during deep subduction based on fluid inclusions. *Am. Mineral.* **100**, 352–377 (2015).
29. M. L. Frezzotti, Diamond growth from organic compounds in hydrous fluids deep within the Earth. *Nat. Comm.* **10**, 4952 (2019).
30. S. Facq, I. Daniel, G. Montagnac, H. Cardon, D. A. Sverjensky, In situ Raman study and thermodynamic model of aqueous carbonate speciation in equilibrium with aragonite under subduction zone conditions. *Geochim. Cosmochim. Acta.* **132**, 375–390 (2014).
31. D. A. Sverjensky, F. Huang, Diamond formation due to a pH drop during fluid–rock interactions. *Nat. Comm.* **6**, 8702 (2015).
32. M. Guild, E. L. Shock, Predicted speciation of carbon in subduction zone fluids, in *Carbon in Earth's Interior* (AGU Publications, 2020), pp. 285–302.
33. R. C. Newton, C. E. Manning, Solubility of anhydrite, $CaSO_4$, in NaCl–H_2O solutions at high pressures and temperatures: Applications to fluid–rock interaction. *J. Petrol.* **46**, 701–716 (2005).
34. J. J. Ague, S. Tassara, M. E. Holycross, J. L. Li, E. Cottrell, E. M. Schwarzenbach, C. Fassoulas, T. John, Slab-derived devolatilization fluids oxidized by subducted metasedimentary rocks. *Nat. Geosci.* **15**, 320–326 (2022).
35. T. Plank, C. E. Manning, Subducting carbon. *Nature* **574**, 343–352 (2019).
36. X. Zhong, M. E. Galvez, The subducting slab as a chromatographic column: Regimes of sub-solidus mass transport as a function of lithospheric hydration state, with special reference to the fate of carbonate. *J. Geophys. Res. Solid Earth* **127**, e2021JB023851 (2022).
37. P. D. Clift, A revised budget for Cenozoic sedimentary carbon subduction. *Rev. Geophys.* **55**, 97–125 (2017).
38. S. Ferrando, C. Groppo, M. L. Frezzotti, D. Castelli, A. Proyer, Dissolving dolomite in a stable UHP mineral assemblage: Evidence from Cal-Dol marbles of the Dora-Maira Massif (Italian Western Alps). *Am. Mineral.* **102**, 42–60 (2017).
39. A. Maffeis, S. Ferrando, J. .A. D. Connolly, C. Groppo, M. L. Frezzotti, D. Castelli, Thermodynamic analysis of HP-UHP fluid inclusions: The solute load and chemistry of metamorphic fluids. *Geochim. Cosmochim. Acta.* **315**, 207–229 (2021).
40. A. Maffeis, S. Ferrando, J. .A. D. Connolly, M. L. Frezzotti, D. Castelli, Fluid redox fingerprint of the $CaCO_3$ + antigorite dehydration reaction in subducted metacarbonate sediments. *Geosci.* **13**, 130 (2023).
41. D. Canil, S. A. Fellows, Sulphide–sulphate stability and melting in subducted sediment and its role in arc mantle redox and chalcophile cycling in space and time. *Earth Planet. Sci. Lett.* **470**, 73–86 (2017).
42. G. S. Pokrovski, J. Dubessy, Stability and abundance of the trisulfur radical ion S_3^- in hydrothermal fluids. *Earth Planet. Sci. Lett.* **411**, 298–309 (2015).
43. K. A. Evans, Redox decoupling and redox budgets: Conceptual tools for the study of earth systems. *Geology* **34**, 489 (2006).

44. A. G. Tomkins, K. A. Evans, Separate zones of sulfate and sulfide release from subducted mafic oceanic crust. *Earth Planet. Sci. Lett.* **428**, 73–83 (2015).
45. S. Tumiati, N. Malaspina, Redox processes and the role of carbon-bearing volatiles from the slab–mantle interface to the mantle wedge. *J. Geol. Soc. London* **176**, 388–397 (2019).
46. V. J. Salters, A. Stracke, Composition of the depleted mantle. *Geochem. Geophys. Geosystems.* **5**, 2003GC000597 (2004).
47. V. Stagno, D. O. Ojwang, C. A. McCammon, D. J. Frost, The oxidation state of the mantle and the extraction of carbon from Earth's interior. *Nature* **493**, 84–88 (2013).
48. K. A. Evans, The redox budget of subduction zones. *Earth Sci. Rev.* **113**, 11–32 (2012).
49. J. Muñoz-Montecinos, W. M. Behr, Transient permeability of a deep-seated subduction interface shear zone. *Geophys. Res. Lett.* **50**, e2023GL104244 (2023).
50. Y. Cao, S. G. Song, Y. L. Niu, H. Jung, Z. M. Jin, Variation of mineral composition, fabric and oxygen fugacity from massive to foliated eclogites during exhumation of subducted ocean crust in the North Qilian suture zone, NW China. *J. Metamorph. Geol.* **29**, 699–720 (2011).
51. Y. Liu, M. Santosh, T. Yuan, H. Li, T. Li, Reduction of buried oxidized oceanic crust during subduction. *Gondw. Res.* **32**, 11–23 (2016).
52. C. Spandler, C. Pirard, Element recycling from subducting slabs to arc crust: A review. *Lithos* **170-171**, 208–223 (2013).
53. F. Crameri, V. Magni, M. Domeier, G. E. Shephard, K. Chotalia, G. Cooper, C. M. Eakin, A. G. Grima, D. Gürer, Á. Király, E. Mulyukova, K. Peters, B. Robert, M. Thielmann, A transdisciplinary and community-driven database to unravel subduction zone initiation. *Nat. Commun.* **11**, 3750 (2020).
54. M. W. Schmidt, S. Poli. Generation of mobile components during subduction of oceanic crust, in *Treatise on Geochemistry*, H. D. Holland, K. K. Turekian, Eds. (Elsevier, 2003), pp. 567–591.
55. E. Cannaò, N. Malaspina, From oceanic to continental subduction: Implications for the geochemical and redox evolution of the supra-subduction mantle. *Geosphere* **14**, 2311–2336 (2018).
56. S. Turner, J. U. Foden, U, Th and Ra disequilibria, Sr, Nd and Pb isotope and trace element variations in Sunda arc lavas: Predominance of a subducted sediment component. *Contrib. to Mineral. Petrol.* **142**, 43–57 (2001).
57. R. Avanzinelli, J. Prytulak, S. Skora, A. Heumann, G. Koetsier, T. Elliott, T. Combined, Combined ^{238}U–^{230}Th and ^{235}U–^{231}Pa constraints on the transport of slab-derived material beneath the Mariana Islands. *Geochim. Cosmochim. Acta.* **92**, 308–328 (2012).
58. T. Stachel, R. W. Luth, Diamond formation—Where, when and how? *Lithos* **220**, 200–220 (2015).
59. J. A. Padrón-Navarta, V. L. Sánchez-Vizcaíno, M. D. Menzel, M. T. Gómez-Pugnaire, C. J. Garrido, Mantle wedge oxidation from deserpentinization modulated by sediment-derived fluids. *Nat. Geosci.* **16**, 268–275 (2023).
60. J. A. D. Connolly, M. E. Galvez, Electrolytic fluid speciation by Gibbs energy minimization and implications for subduction zone mass transfer. *Earth Planet. Sc. Lett.* **501**, 90–102 (2018).
61. T. J. B. Holland, R. Powell, An improved and extended internally consistent thermodynamic dataset for phases of petrological interest, involving a new equation of state for solids. *J. Metam. Geol.* **29**, 333–383 (2011).
62. D. A. Sverjensky, B. Harrison, D. Azzolini, Water in the deep Earth: The dielectric constant and the solubilities of quartz and corundum to 60kb and 1200°C. *Geochim. Cosmochim. Acta.* **129**, 125–145 (2014).
63. K. S. Pitzer, S. M. Sterner, Equations of state valid continuously from zero to extreme pressures for H_2O and CO_2. *J. Chem. Phys.* **101**, 3111–3116 (1994).
64. R. de Santis, G. J. F. Breedveld, J. M. Prausnitz, Thermodynamic properties of aqueous gas mixtures at advanced pressures. *Ind. Eng. Chem. Process Des. Dev.* **13**, 374–377 (1974).
65. M. E. Galvez, C. E. Manning, J. A. D. Connolly, D. Rumble, The solubility of rocks in metamorphic fluids: A model for rock-dominated conditions to upper mantle pressure and temperature. *Earth Planet. Sc. Lett.* **430**, 486–498 (2015).
66. P. B. Kelemen, J. L. Rilling, E. M. Parmentier, L. Mehl, B. R. Hacker, Thermal structure due to solid-state flow in the mantle wedge beneath arcs. *Geophys. Monogr. Ser.* **138**, 293–311 (2003).
67. F. A. Davis, J. A. Tangeman, T. J. Tenner, M. M. Hirschmann, The composition of KLB-1 peridotite. *Am. Mineral.* **94**, 176–180 (2009).
68. A. C. Ganzhorn, H. Pilorgé, B. Reynard, Porosity of metamorphic rocks and fluid migration within subduction interfaces. *Earth Planet. Sci. Lett.* **522**, 107–117 (2019).
69. R. L. McGary, P. E. Evans, J. Wannamaker, S. Elsenbeck, S. Rondenay, Pathway from subducting slab to surface for melt and fluids beneath Mount Rainier. *Nature* **511**, 338–340 (2014).
70. P. E. van Keken, B. R. Hacker, E. M. Syracuse, G. A. Abers, Subduction factory: 4. Depth-dependent flux of H_2O from subducting slabs worldwide. *J. Geophys. Res. Solid Earth* **116**, 2010JB007922 (2011).
71. T. M. Boundy, C. L. Donohue, E. J. Essene, K. Mezger, H. Austrheim, Discovery of eclogite facies carbonate rocks from the Lindås Nappe, Caledonides, Western Norway. *J. Metamorph. Geol.* **20**, 649–667 (2002).
72. K. A. Evans, A. G. Tomkins, The relationship between subduction zone redox budget and arc magma fertility. *Earth Planet. Sci. Lett.* **308**, 401–409 (2011).
73. M. Le Voyer, K. A. Kelley, E. Cottrell, E. H. Hauri, Heterogeneity in mantle carbon content from CO_2-undersaturated basalts. *Nat. Commun.* **8**, 14062 (2017).
74. A. Aiuppa, F. Casetta, M. Coltorti, V. Stagno, G. Tamburello, Carbon concentration increases with depth of melting in Earth's upper mantle. *Nat. Geosci.* **14**, 697–703 (2021).
75. G. H. Gudfinnsson, D. C. Presnall, Continuous gradations among primary carbonatitic, kimberlitic, melilititic, basaltic, picritic, and komatiitic melts in equilibrium with garnet lherzolite at 3–8 GPa. *J. Petrol.* **46**, 1645–1659 (2005).
76. R. D. Jarrard, Subduction fluxes of water, carbon dioxide, chlorine, and potassium. *Geochem. Geophys. Geosystems.* **4**, 2002GC000392 (2003).
77. C. Groppo, S. Ferrando, M. Gilio, S. Botta, F. Nosenzo, G. Balestro, A. Festa, F. Rolfo, What's in the sandwich? New *P–T* constraints for the (U) HP nappe stack of southern Dora-Maira Massif (Western Alps). *Eur. J. Mineral.* **31**, 665–683 (2019).
78. E. M. Syracuse, P. E. van Keken, G. A. Abers, The global range of subduction zone thermal models. *Phys. Earth Planet. In.* **183**, 73–90 (2010).
79. S. C. Penniston-Dorland, M. J. Kohn, C. E. Manning, The global range of subduction zone thermal structures from exhumed blueschists and eclogites: Rocks are hotter than models. *Earth Planet. Sci. Lett.* **428**, 243–254 (2015).
80. L. N. Warr, IMA–CNMNC approved mineral symbols. *Mineral. Mag.* **85**, 291–320 (2021).
81. S. Lallemand, D. Arcay, Subduction initiation from the earliest stages to self-sustained subduction: Insights from the analysis of 70 Cenozoic sites. *Earth Sci. Rev.* **221**, 103779 (2021).

Acknowledgments: Part of this paper is part of A.M.'s PhD thesis. We are grateful to the anonymous reviewers for constructive comments that greatly improved the manuscript. **Funding:** This work was supported by Italian Ministry of University and Research (PRIN 2022, project no. 2022HA8XCS) to M.L.F., and University of Turin (FERS_RILO_19-22) to S.F. **Author contributions:** Conceptualization: A.M., M.L.F., and S.F. Methodology: A.M. and J.A.D.C. Software: J.A.D.C. Formal analysis: A.M. Investigation: A.M. and M.L.F. Visualization: A.M. Supervision: A.M., S.F., J.A.D.C., M.L.F., and D.C. Writing—original draft: A.M. and M.L.F. Writing—review and editing: All the authors. Funding acquisition: M.L.F. and S.F. **Competing interests:** The authors declare that they have no competing interests. **Data and materials availability:** All data needed to evaluate the conclusions in the paper are present in the paper and/or the Supplementary Materials.

Submitted 16 June 2023
Accepted 15 February 2024
Published 20 March 2024
10.1126/sciadv.adj2770